

RESEARCH ARTICLE | AUGUST 22 2023

Persistent homology-based descriptor for machine-learning potential of amorphous structures

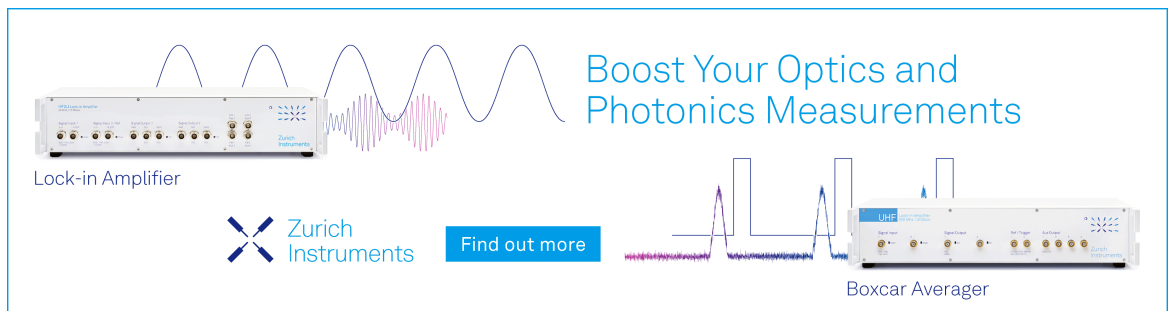
Emi Minamitani ; Ippei Obayashi ; Koji Shimizu ; Satoshi Watanabe 



J. Chem. Phys. 159, 084101 (2023)


<https://doi.org/10.1063/5.0159349>

 CHORUS



Boost Your Optics and Photonics Measurements

Lock-in Amplifier

 Zurich Instruments

[Find out more](#)

Boxcar Averager

Persistent homology-based descriptor for machine-learning potential of amorphous structures

Cite as: J. Chem. Phys. 159, 084101 (2023); doi: 10.1063/5.0159349

Submitted: 23 May 2023 • Accepted: 18 July 2023 •

Published Online: 22 August 2023



View Online



Export Citation



CrossMark

Emi Minamitani,^{1,2,3,a)}  Ippei Obayashi,^{3,4,b)}  Koji Shimizu,^{5,c)}  and Satoshi Watanabe^{5,d)} 

AFFILIATIONS

¹The Institute of Scientific and Industrial Research, Osaka University, Ibaraki 567-0047, Japan

²Institute for Molecular Science, Okazaki 444-8585, Japan

³JST, PRESTO, Kawaguchi, Saitama 332-0012, Japan

⁴Center for Artificial Intelligence and Mathematical Data Science, Okayama University, Okayama 700-8530, Japan

⁵Department of Materials Engineering, The University of Tokyo, Hongo, Bunkyo 113-8656, Japan

^{a)} Author to whom correspondence should be addressed: eminamitani@sanken.osaka-u.ac.jp

^{b)} i.obayashi@okayama-u.ac.jp

^{c)} shimizu@cello.t.u-tokyo.ac.jp

^{d)} watanabe@cello.t.u-tokyo.ac.jp

ABSTRACT

High-accuracy prediction of the physical properties of amorphous materials is challenging in condensed-matter physics. A promising method to achieve this is machine-learning potentials, which is an alternative to computationally demanding *ab initio* calculations. When applying machine-learning potentials, the construction of descriptors to represent atomic configurations is crucial. These descriptors should be invariant to symmetry operations. Handcrafted representations using a smooth overlap of atomic positions and graph neural networks (GNN) are examples of methods used for constructing symmetry-invariant descriptors. In this study, we propose a novel descriptor based on a persistence diagram (PD), a two-dimensional representation of persistent homology (PH). First, we demonstrated that the normalized two-dimensional histogram obtained from PD could predict the average energy per atom of amorphous carbon at various densities, even when using a simple model. Second, an analysis of the dimensional reduction results of the descriptor spaces revealed that PH can be used to construct descriptors with characteristics similar to those of a latent space in a GNN. These results indicate that PH is a promising method for constructing descriptors suitable for machine-learning potentials without hyperparameter tuning and deep-learning techniques.

© 2023 Author(s). All article content, except where otherwise noted, is licensed under a Creative Commons Attribution (CC BY) license (<http://creativecommons.org/licenses/by/4.0/>). <https://doi.org/10.1063/5.0159349>

I. INTRODUCTION

High-accuracy prediction of the physical properties of disordered systems such as amorphous materials is significantly challenging in condensed-matter physics. *Ab initio* calculations, based on quantum mechanics, are versatile and highly accurate. However, the substantial computational cost limits the application of these calculations to realistic amorphous structures. In recent years, machine-learning potentials have emerged as an attractive method to resolve the trade-off between computational cost and accuracy.

Machine-learning potential involves the construction of a surrogate model of the relationship between atomic coordinates and

physical properties, which provides an alternative to computationally intensive *ab initio* calculations. Various machine-learning models have been developed over the past decade, including Gaussian process regression,^{1,2} artificial neural networks,^{3–6} and their derivatives.^{7–12} A key requirement of machine-learning potential models is the development of a suitable method for converting atomic coordinates into vector data.

Predictions derived from machine-learning potentials should adhere to physical laws. For example, the total energy of a system is invariant to the spatial translation, rotation, reflection, and permutation of chemically equivalent atoms. A direct approach to achieve this is to ensure that the vectorial inputs of the machine-learning

potential remain invariant under these symmetry operations. Currently, two methods exist for creating vectorial representations of atomic coordinates, which are commonly known as descriptors. The first method involves using handcrafted feature representations such as the smooth overlap of atomic positions (SOAP)¹³ and atom-centered symmetry functions.¹⁴ The second method uses graph neural networks (GNN),^{5,6,11,12} where essential structural characteristics are extracted by neural networks during training. Using the former descriptors, even a simple machine-learning model can adequately perform predictions. However, the optimal values of numerous hyperparameters in the descriptor, such as the cutoff, shape, and size of the basis functions, should be determined. The latter method has the advantage of not requiring descriptor hyperparameter tuning, but it requires increased model complexity.

This study proposes a descriptor that differs from the aforementioned approaches, which eliminates the need for hyperparameter tuning while predicting the energies of amorphous materials using a simple machine-learning model. In this study, we focus on persistent homology (PH),^{15,16} a recently developed computational topology technique. PH effectively extracts topological and geometrical characteristics and has been applied to structural analyses in wide-ranging fields, from glass to bio-related materials.^{17–22} In addition, recent studies have demonstrated that PH effectively identifies correlations between the physical and structural properties of materials.^{23–29}

Herein, we provide a brief overview of the fundamental concepts of PH. In mathematics, a shape is considered a topological space, X , consisting of a set of points (in our case, atoms) and a topology. The topological characteristics of X are represented by holes in space that are encoded in an algebraic structure called the k -th homology group $H_k(X)$. A nested sequence of topological space, $X_1 \subseteq X_2 \subseteq \dots \subseteq X_n$, results in the series $H_k(X_1), H_k(X_2) \dots H_k(X_n)$. The concept of PH involves monitoring the elements of $H_k(X_i)$ as i increases, where i represents the scale and is often referred to as “time.” The procedure used to obtain this sequence is called *filtration* and is illustrated in Fig. 1.

During the filtration process for the first homology in a two-dimensional system, circles with a radius r are placed at the respective atoms. Subsequently, r is increased gradually. Consequently, the circles begin to intersect, and then, edges are set between the centers of the intersecting circles. The growing network formed by these edges defines the sequence of the topological space, X_i . A closed path formed by these edges corresponds to a topological feature called a *cycle*. As the radius continues to increase, the closed path becomes completely covered by circles, which is interpreted as the conversion of the cycle into another type of topological feature called a *boundary*. The features of PH are represented by pairs of birth and death times at which cycles appear and are converted into boundaries. Filtration can be generalized into three or more dimensions using spheres or hyperspheres. A two-dimensional visualization of birth–death time pairs is known as a persistence diagram (PD).

Based on this definition, the PD captures information regarding the bonding state and distribution of atoms and remains invariant to the spatial translation, rotation, reflection, and permutations of chemically equivalent atoms. Moreover, PD does not require any hyperparameter to be adjusted manually.

In this study, we demonstrate that PH can be used as an input for the machine-learning potential of amorphous structures. The specific target is amorphous carbon (aC). Initially, we demonstrate that the normalized two-dimensional histogram derived from the PD can predict the average energy per atom of aC at various densities, even when using a Ridge model. Moreover, we demonstrate that the prediction accuracy is improved by utilizing a convolutional neural network (CNN) model. Subsequently, we compare the PH descriptors, conventional handcrafted descriptors, and latent space of the GNN-based architectures. SOAP descriptors are selected for the conventional handcrafted descriptor, whereas SchNet is used for the GNN-based architecture. We reveal the differences in how each descriptor captures structural characteristics. The 2D maps obtained from the dimensionality reduction of the PH descriptors resemble those of the SchNet descriptors but differ from those of the SOAP descriptors. Based on these results, we conclude that PH can construct descriptors with characteristics similar to those of a latent space in a GNN, without deep learning and hyperparameter tuning.

II. METHODS

A. Datasets

The aC dataset was generated by *ab initio* calculations using the VASP software.^{30–33} We utilized the local-density approximation (LDA) exchange–correlation functional and PAW potential for carbon. Melt-quench simulations were performed to generate amorphous and liquid-state structures. A simple cubic lattice with 216 carbon atoms was selected as the initial state. Simulations were conducted at densities of 1.5, 1.7, 2.0, 2.2, 2.4, 2.6, 2.8, 3.0, 3.2, 3.4, and 3.5 g/cm³ to generate different structures. The NVT ensemble^{34,35} was used for all the melt-quench simulations, and density was adjusted by varying the size of the simulation cell. A time step of 1 fs was used for the simulations. For all densities, only the Γ points were sampled in k-space. To increase the structural diversity, six independent simulations were performed.

During the melt-quench simulations, the temperature was increased from 300 to 9000 K in 2 ps to melt the carbon. Equilibrium molecular dynamics (MD) was conducted at 9000 K for 3 ps to form the liquid state, followed by a decrease in temperature to 5000 K in 2 ps and equilibration for 2 ps. Finally, the temperature was decreased from 5000 to 300 K in 2 ps to generate the amorphous structure. During this process, 30 snapshots were obtained from the equilibrium MD trajectory at 9000 K, 100 from the cooling process between 9000 and 5000 K, 25 from the equilibrium MD trajectory at 5000 K, and 100 from the cooling process between 5000 and 300 K, yielding 16 830 data points. The coordination number analysis of this dataset confirms that the carbon atom neighbor environments are adequately diverse (Fig. S2).

Additionally, the data for diamond structures containing 216 atoms at densities of 2.4, 2.6, 2.8, 3.0, 3.2, 3.4, and 3.5 g/cm³ were prepared. Further data on the diamond structures were obtained from the 80 snapshots of the 2 ps equilibrium MD trajectory at 300 K, yielding 560 data points.

To validate the predictions for larger structures, we generated the data for 512-atom systems using the same procedure as that for the 216-atom systems. A single simulation was conducted for each

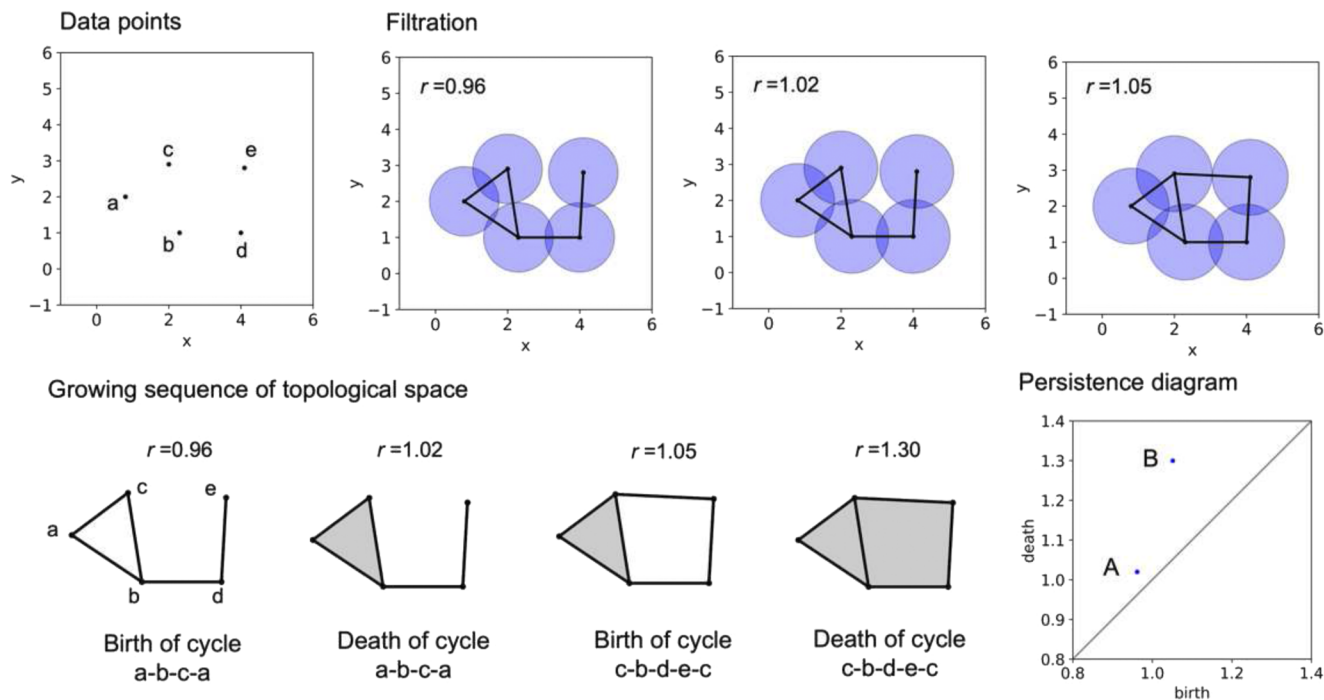


FIG. 1. Schematic of the filtration procedure used to obtain PD from the data points. In this example, there are five points (a)–(e). The PH group obtained by filtration is represented by two birth–death pairs, A and B, in the PD. Values of birth and death time are 0.96 and 1.02 for A and 1.05 and 1.30 for B, respectively. Pair A (B) corresponds to the birth and death of the cycle defined by the closed path a-b-c-a (c-b-d-e-c). The gray-shaded polygon in the growing sequence of the topological space indicates that the closed path formed by the edges of the polygon is completely covered by circles during the filtration process.

density. The number of data points was 2805 for the amorphous and liquid states. These datasets can be downloaded from Zenodo (DOI: <https://doi.org/10.5281/zenodo.7905585>).

B. Persistent homology

In this study, we utilized the HomCloud code^{36,37} to analyze the PH of the amorphous models. Herein, we focused on the ring structures that correspond to the cycles from one-dimensional homology. The birth and death times of the respective cycles were determined by alpha complex filtration. The basic procedure of alpha complex filtration is the same as that depicted in Fig. 1, although the area covered by each sphere is restricted within the Voronoi cell. The radii of the spheres were continuously and uniformly increased from zero until the filtration was completed (i.e., all cycles were converted to boundaries). In accordance with the convention, we denote the birth and death times using the squared values of the radii of the spheres employed during the filtration process. Consequently, the results of these measurements are given in the units of Å^2 .

To create the input for the machine-learning potential, we converted the PDs into two-dimensional histograms using a 128×128 mesh. The square region of $[0.0, 8.0]_{\text{birth}} \times [0.0, 8.0]_{\text{death}}$ in the histogram was targeted. Unlike the previously proposed methods,^{38,39} our method does not either apply a small weight to or remove the birth–death time pairs close to the diagonal line in PD. This is because we expect that the importance of each birth–death

time pair will be automatically recognized during the machine learning process. Because the PD represents the number and size of ring structures, the histogram values depend on the system size. Consequently, the histogram was transformed into a probability distribution, and z-score was standardized to ensure that the descriptors were independent of model size. Because of the small size of the model, periodic boundary conditions (PBC) were applied when calculating the PDs. We discuss the limitations originating from the use of PBC in Sec. 3 of the supplementary material.

By tracing the filtration procedure, we can identify the candidates of the cycle corresponding to each birth–death pair. This enabled inverse analysis of PH, which was used to determine the atomic arrangements corresponding to the low- and high-energy regions. In some cases, several candidates exhibit equivalent topological characteristics. Various approaches^{40,41} exist for selecting a representative cycle for these cases. In this study, the stable volume method⁴¹ was selected, which provides the tightest cycles with robustness against noise.

C. SOAP descriptors

The SOAP descriptors were calculated using DScribe.⁴² The hyperparameters for the SOAP descriptor include the cutoff radius (rcut), number of radial basis functions (nmax), maximum degree of spherical harmonics (lmax), and standard deviation of the Gaussian function used to expand the atomic density (sigma). Optuna⁴³

was used to search for the optimal hyperparameter values, which were determined to be $\text{rcut} = 4.1$, $\text{nmax} = 8$, $\text{lmax} = 9$, and $\text{sigma} = 0.16$ (see Fig. S1 in the supplementary material). These hyperparameters resulted in a SOAP descriptor dimension of 360. The average value across the axis representing the number of atoms was used to evaluate the descriptor space.

D. SchNet

SchNet⁵ was selected as a representative model of the neural network potential based on GNN. SchNetPack⁴⁴ was used to implement the SchNet architecture. SchNet comprises four primary components, as illustrated in Fig. 2 of Ref. 5: Atom embedding, atom-wise layers, interaction blocks, and continuous-filter convolution with filter-generating networks. In SchNet, a set of feature vectors $\mathbf{X}^0 = (\mathbf{x}_1^0, \mathbf{x}_2^0, \dots, \mathbf{x}_n^0)$ for the respective atoms was generated using an atom-embedding layer based on the chemical species of

the atoms. Here, n denotes the number of atoms. Embeddings were initialized randomly. The feature vector \mathbf{X}^0 was updated by passing through each component layer. The feature vectors at the l th layer are denoted by $\mathbf{X}^l = (\mathbf{x}_1^l, \mathbf{x}_2^l, \dots, \mathbf{x}_n^l)$. In addition to these feature vectors, a vector representing the local environment of each atom was constructed within the interaction blocks using filter generation networks based on the distance between the central atom i and the neighboring atom j . The k th element of the vector is defined as

$$e_k(\mathbf{r}_i - \mathbf{r}_j) = \exp(-\gamma(\|\mathbf{r}_i - \mathbf{r}_j\| - \mu_k)^2), \quad (1)$$

where μ_k represents the center of the Gaussian function. In this study, γ was set to 0.1 \AA^{-2} and μ_k to 60 different values at equal intervals in the range of 0–5 Å, yielding a 60-dimensional vector. Subsequently, this vector was passed to a fully connected neural network

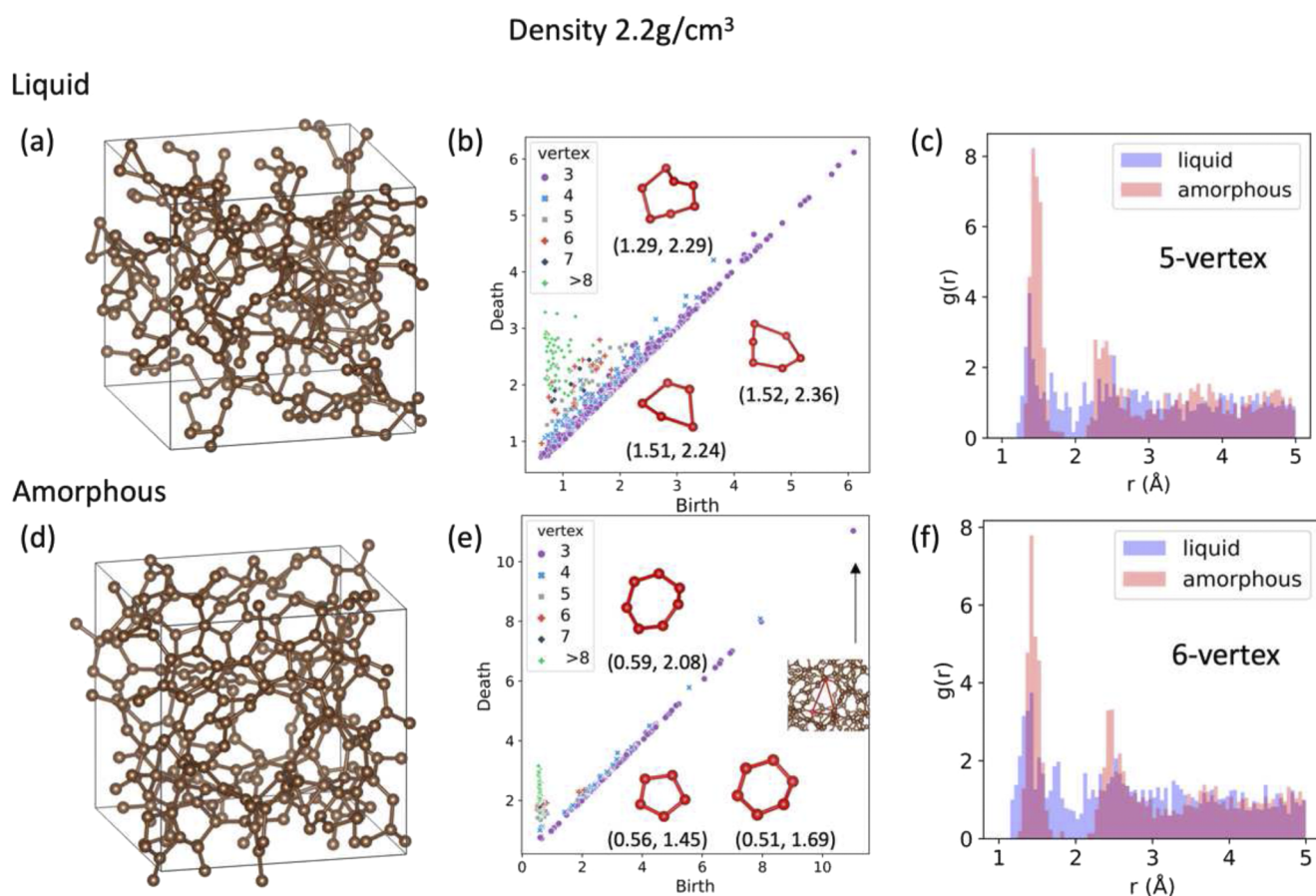


FIG. 2. Structures, PDs, and results of stable volume analysis for liquid and amorphous carbon with a density of 2.2 g/cm^3 . (a) and (d) show the structural models of the liquid and amorphous phases, respectively. (b) and (e) present the PDs derived from the liquid and amorphous structures, respectively. The colors and styles of the symbols in these figures signify the number of vertices in the cycles corresponding to each point. The insets in these figures depict typical ring structures of five-, six-, and seven-vertex cycles, as well as the cycle with the largest birth time in the amorphous structure. The pairs of numbers under five-, six-, and seven-vertex cycles represent the birth and death times of each cycle. (c) and (f) display the results of the calculation of the radial distribution function restricted to the five- and six-vertex cycles in the liquid and amorphous structures, respectively.

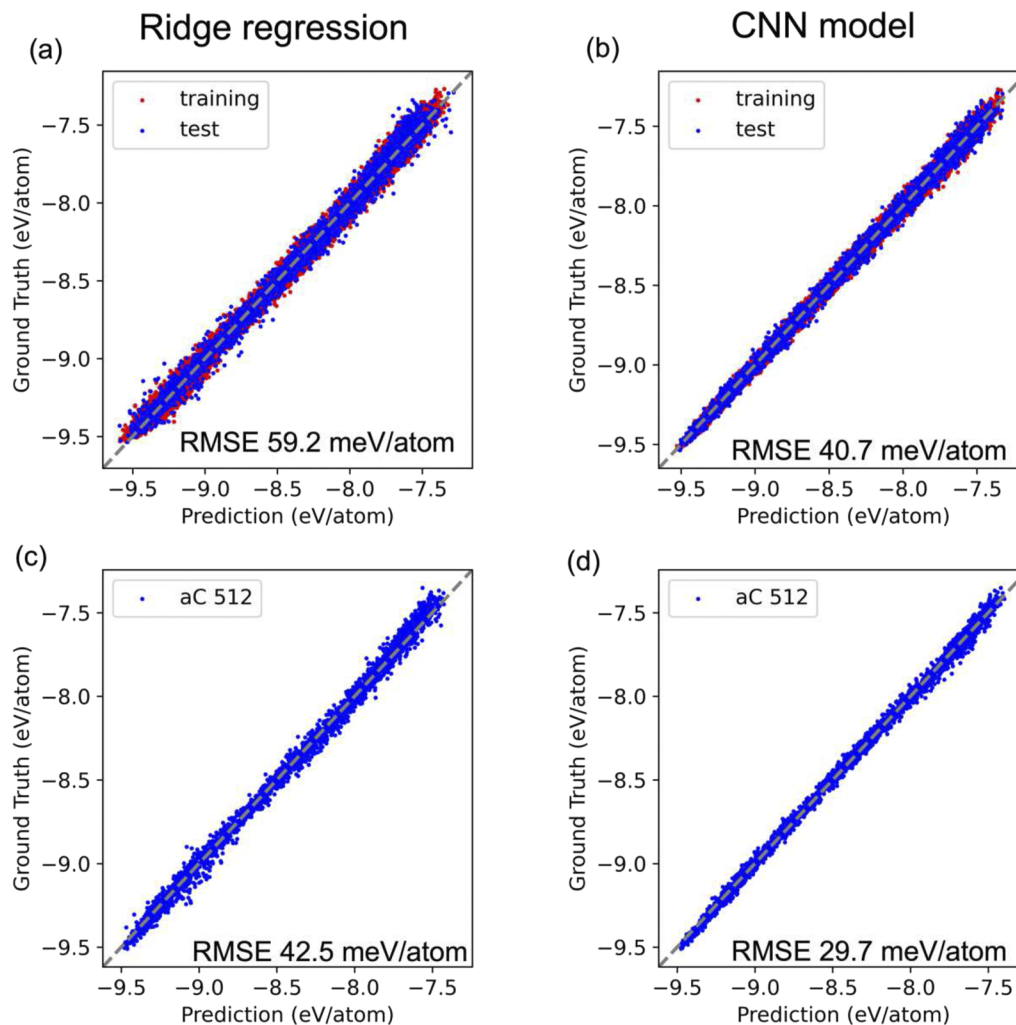


FIG. 3. Calculation results and predictions by the machine-learning model based on PH descriptors: Training and test results of the mean energies per atom in aC. The red dots represent the comparison results for the test data, while the blue dots represent those for the training data. Results from the (a) Ridge regression and (b) CNN models are shown, along with (c) and (d) their predictions of the mean energies per atom for larger aC systems, respectively.

to produce an output vector, $W^l(r_i - r_j)$. The interaction of atoms incorporated by a continuous-filter convolution is defined as

$$\mathbf{x}_i^{l+1} = \sum_{j \in N(i)} \mathbf{x}_j^l \circ W^l(r_i - r_j), \quad (2)$$

where $N(i)$ represents the set of neighbors of atoms i .

By updating the learnable weight parameters in the architecture with a combination of the four components during the training procedure, the network generated descriptors that capture the structural characteristics to determine the total energy. In this study, the output from the last interaction block of the trained SchNet model was considered the descriptor generated by SchNet. Because the descriptors were computed for each atom, the resulting descriptors formed an $n \times D$ matrix, where D represents the descriptor dimension that was set to 100. To evaluate the descriptor space, the average value of

the D -dimensional vector along the axis of the number of atoms was used.

E. Ridge regression

Ridge regression for the total energies, based on the PD-generated descriptors, was conducted using the Scikit-learn package.⁴⁵ An intercept term was included in all the regression models. Because all the input values were non-negative, the regression coefficient was directly interpreted. The regularization parameter was set to 200.0.

F. CNN model

The CNN model was implemented using PyTorch.⁴⁶ The model comprises three convolution layers followed by max-pooling

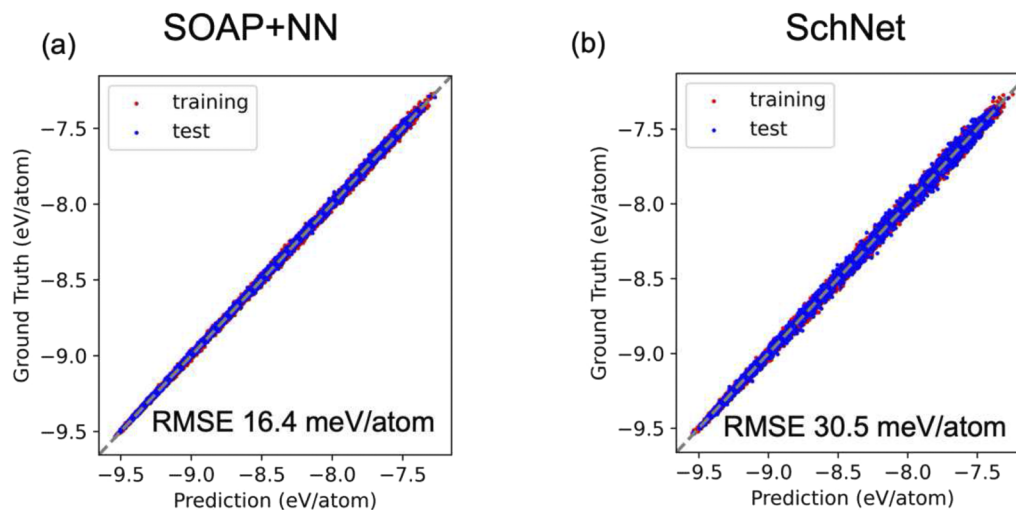


FIG. 4. Calculation results and predictions by the machine-learning model based on the SOAP descriptor and SchNet. Training and test results of the mean energies per atom in aC with red (blue) dots representing the comparison results for the test (training) data. Results obtained by (a) the NN based on SOAP descriptors and (b) the SchNet model.

layers and two fully connected layers. The ReLU function was used as the activation function in the model. The channel size of the first two convolution layers was 64, whereas that of the last layer was 32. The filter size was 3×3 for all the convolution layers.

During the training process, the loss function was evaluated based on the mean squared error between the predicted and actual mean energy per atom. The weights and biases in the convolution and fully connected layers were optimized using stochastic gradient descent (SGD) with a Nesterov momentum of 0.9 and a weight decay of 0.001. The milestones were set at 200, 400, 800, and 1200, and the number of epochs was set to 1600. When the epoch reached the milestones, the learning rate was reduced by a factor of 0.5. The initial value of the learning rate was set to 0.0015.

G. Neural network potential based on SOAP descriptors

Neural network potentials based on SOAP descriptors were implemented using PyTorch. The model consists of two fully connected hidden layers with 40 nodes in each layer. During the training process, the loss function was evaluated based on the mean squared error between the predicted and actual mean energy per atom. The weights and biases in the model were optimized using the Adam optimizer. The milestones were set at 200, 500, and 1000, and the number of epochs was set to 2000. When the epoch reached the milestones, the learning rate was reduced by a factor of 0.5. The initial value of the learning rate was set to 0.001.

III. RESULTS AND DISCUSSION

First, we present the typical PDs for liquid and amorphous carbon. Figures 2(a) and 2(d) show samples of liquid and amorphous structures with a density of 2.2 g/cm^3 . The PDs derived from

these structures are presented in Figs. 2(b) and 2(e). The colors and symbols in these PDs signify the number of vertices of the cycle corresponding to each point, which is determined by stable volume analysis.

The three-vertex cycle with a long birth–death time that is observed only in the amorphous state originates from the pore structure present under low- and medium-density conditions. The local structure corresponding to this cycle is depicted in the inset of Fig. 2(e).

A remarkable difference between the liquid and amorphous states emerges in the birth–death time distributions for cycles with more than five vertices. We present the typical local structure of the five-, six-, and seven-vertex cycles in both liquid and amorphous states in the insets of Figs. 2(b) and 2(e), along with their birth–death times. Compared with the cycles in the amorphous state, those in the liquid state exhibit structures with greater distortion.

In the PD of amorphous structures, these cycles form a vertical line in the birth time range of 0.5–0.7. Such a structure is not observed in the case of liquid. This corresponds to the fact that medium-range order (MRO) exists in amorphous structures but not in the liquid state. This correspondence can be clearly observed in the radial distribution function using ring structures corresponding to five-vertex and six-vertex cycles [Figs. 2(c) and 2(f)].

Although similar differences in the PDs between amorphous and liquid structures also appear in the cases of lower and higher densities, it was found that the area of birth–death times distribution varies with the density (Figs. S5 and S6). These analysis results demonstrate that it is possible to detect the presence or absence of MRO and pore structures from the PD.

Next, we demonstrated that the mean energy per atom in amorphous/liquid carbon can be predicted using PDs. As described in Sec. II, we constructed descriptors based on PH by converting the PDs into two-dimensional histograms. These PH descriptors were used as inputs for the Ridge regression and CNN models.

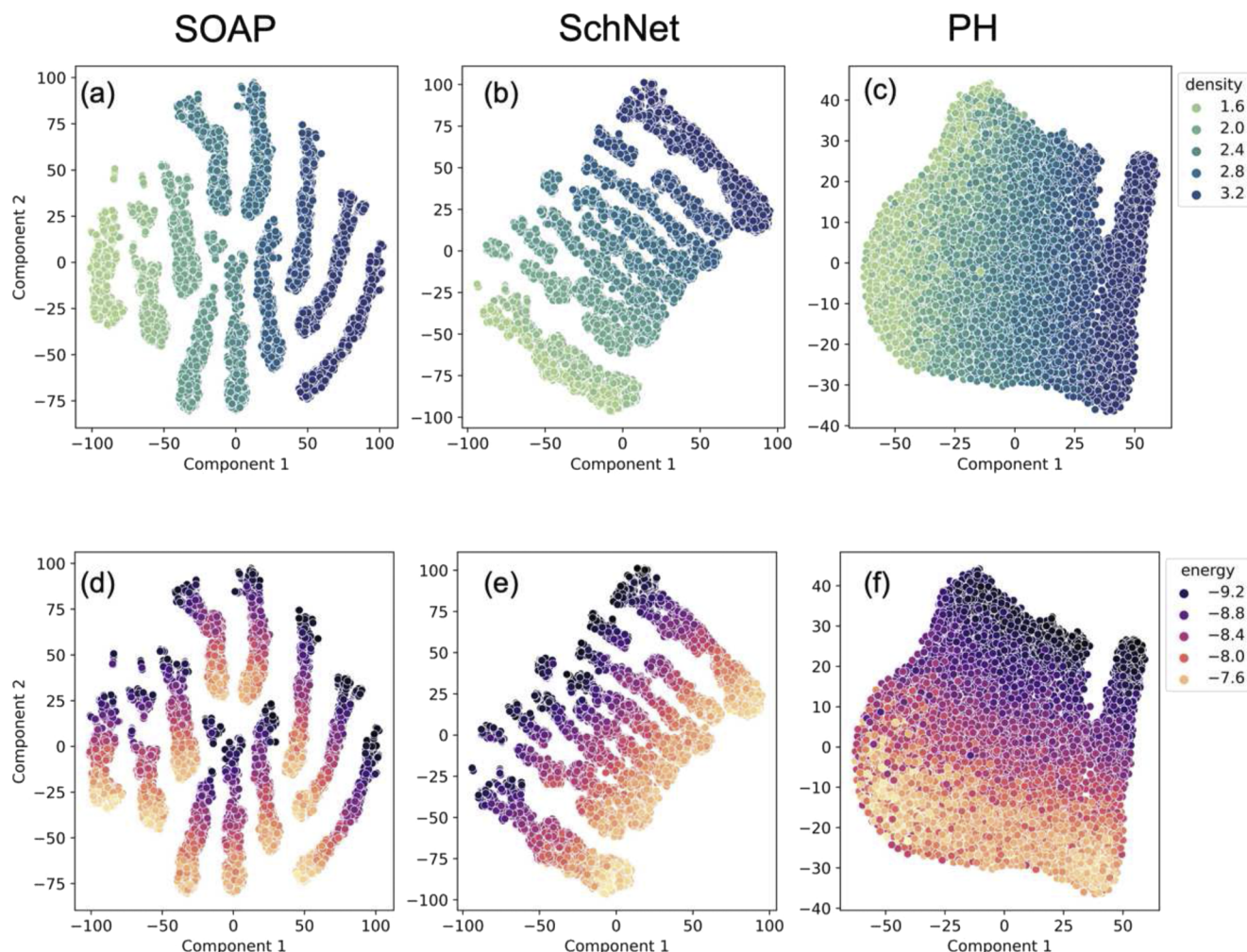


FIG. 5. Dimensionality reduction results obtained by t-SNE for the SOAP, PH, and SchNet descriptors. The perplexity in the t-SNE model is 30.0. In panels (a)–(c), the color of the data points corresponds to the density values, whereas in panels (d)–(f), it corresponds to the energy values.

Figures 3(a) and 3(b) show the training and test results of the respective models for the 216-atom aC system. In this study, 80% of the data were used as training data, and the remaining 20% were used as test data. Even using a simple Ridge regression model, the mean energy per atom in both amorphous and liquid carbon was predicted by the PH descriptors. The root mean squared error (RMSE) for the test data was 59.2 meV/atom. The prediction accuracy improved by utilizing the CNN model, and the RMSE for the test data decreased to 40.7 meV/atom.

As shown in Fig. S7, both ridge regression and CNN predictions were valid when the diamond structures were included in the dataset. This result highlights that the PH descriptors effectively capture the correlation between the atomic structures and the energies of various structures.

Machine-learning potentials should maintain their prediction accuracy when applied to a system larger than that of the training

data. Therefore, we predicted the mean energy per atom in aC for a system with 512 atoms. As shown in Figs. 3(c) and 3(d), both the Ridge regression and CNN models accurately predicted the energies based on the PH descriptor.

Subsequently, we compared these results with those obtained using other methods. SOAP and SchNet were used as examples of a conventional handcrafted representation and GNN model, respectively. Figure 4 shows the results of the training and test for the 216-atom aC system using these methods. Among the investigated models, the combination of the SOAP descriptor and neural network exhibited the highest accuracy, and the RMSE for the test data was 16.4 meV/atom. The prediction accuracy is sensitive to the selection of hyperparameters. As shown in Fig. S8, different hyperparameters can reduce prediction accuracy. For the SchNet model, the RMSE for the test data was 30.5 meV/atom, which falls between those obtained from the SOAP+NN and PH descriptor+CNN models.

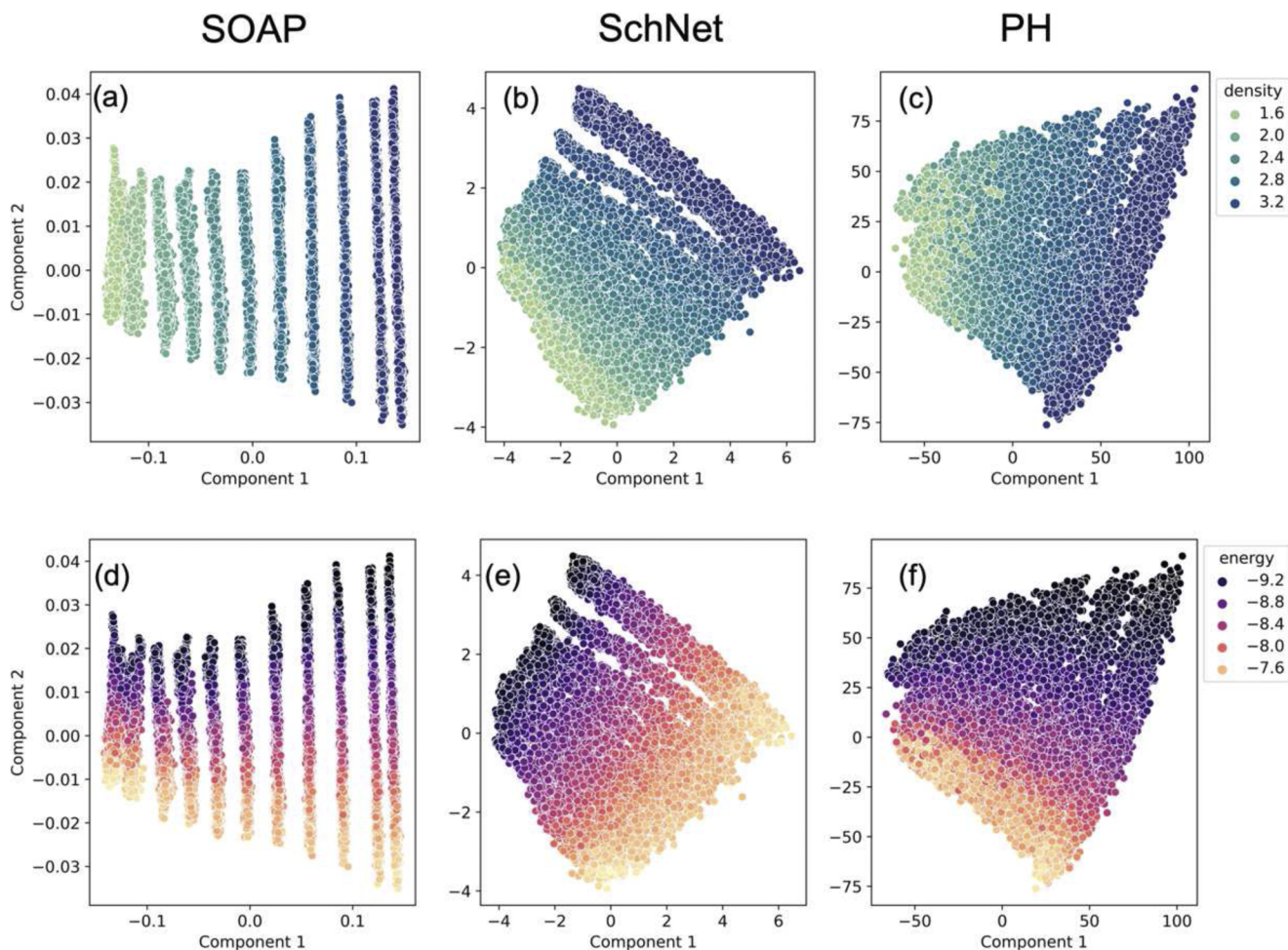


FIG. 6. Dimensionality reduction results obtained by PCA for the SOAP, PH, and SchNet descriptors. In panels (a)–(c), the color of the data points corresponds to the density values, whereas in panels (d)–(f), it corresponds to the energy values.

Note that all these prediction accuracies achieved by machine-learning potentials are superior to those obtained from empirical potentials (Fig. S9).

Beyond the comparison of the prediction accuracy, we investigated how these descriptors capture the structural characteristics of amorphous structures using dimensionality reduction. As described in the Methods section, the average values of the descriptors for the atoms were used to evaluate the descriptor space constructed using SOAP and SchNet. We note that this procedure did not cause a significant loss of information. As shown in Fig. S10, the mean energies per atom were accurately predicted by the averaged descriptors using a neural network. Figure 5 shows the t-SNE analysis results. The colors in Figs. 5(a)–5(c) correspond to the density of aC, whereas those in Figs. 5(d)–5(f) correspond to the energy of aC. In the t-SNE 2D maps of the SOAP descriptor space, descriptors were grouped into discrete island-like structures based on their densities [Fig. 5(a)].

Similarly, the t-SNE 2D maps for SchNet exhibited island-like structures; however, the distribution of each island was broader than

that in the case of SOAP, and several islands partially overlapped [Figs. 5(b) and 5(e)]. The 2D visualizations of the PH descriptor space exhibited the most continuous distributions with respect to both energy and density, as shown in Figs. 5(c) and 5(f). These characteristics of the 2D visualizations were valid when different hyperparameters values were used in the t-SNE analysis (Figs. S11 and S12). Moreover, principal component analysis (PCA) exhibited similar results. As shown in Fig. 6, the 2D visualization of the SOAP descriptor using PCA revealed a discrete distribution, whereas those of the PH and SchNet descriptor spaces were continuous.

Notably, the above-mentioned differences between the SOAP and PH/SchNet descriptors were independent of the hyperparameters used in the SOAP descriptors. As shown in Fig. S13, the dimensionality reduction of the SOAP descriptor used in Fig. S8 had a discrete distribution similar to those shown in Figs. 5 and 6. This indicates that the continuous distribution originated from the additional information captured by the PH and SchNet descriptors but not by the SOAP descriptor. One promising candidate for this

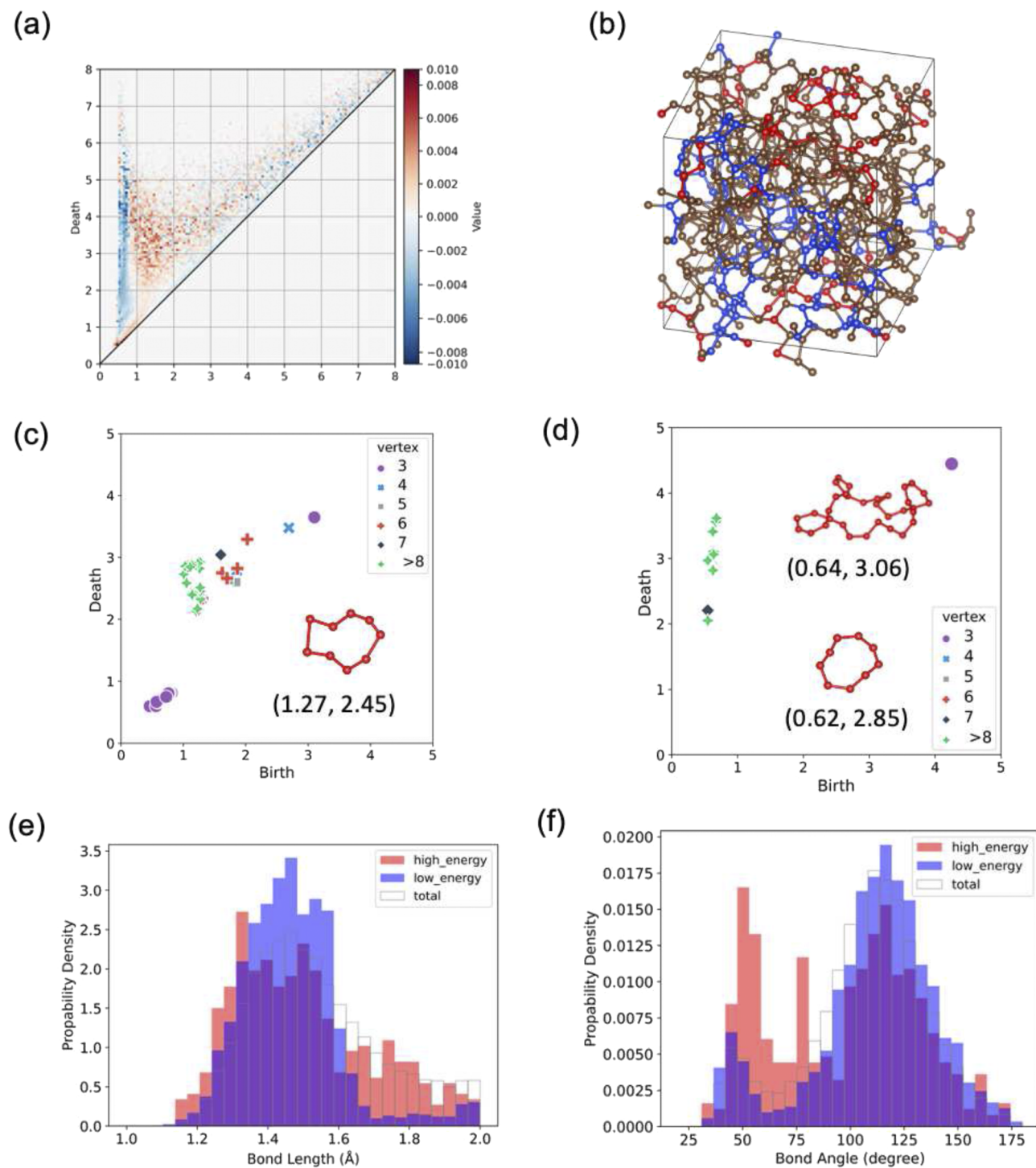


FIG. 7. Inverse analysis results based on the PH descriptor: (a) Projection of the Ridge coefficient onto the mesh grid used to generate the 2D histogram of the PD. (b) Visualization of the high- and low-energy regions in a 512-atom aC sample determined by inverse analysis. (c) and (d) Distribution of the birth-death times for the cycles assigned to high-energy region and low energy region in the structures obtained from MD trajectory at 5000 K with a mass density of 2.4 g/cm^3 , respectively. The insets in these figures depict examples of ring structures. The colors and styles of the symbols in the figures signify the number of vertices of the cycles that correspond to each point. The pair of numbers under the cycles represents the birth and death time of each cycle. (e) and (f) Histograms of the bond lengths and angles in the high- and low-energy regions determined by inverse analysis. Data from 25 samples are aggregated and visualized as histograms.

type of information is the topological structure, which is intrinsically incorporated into PH and GNN.

Based on these results, we concluded that the extraction of structural characteristics by PH is similar to that by GNN, but different from that by SOAP. Thus, PH can construct a descriptor similar to that of a GNN without deep learning and hyperparameter tuning.

These characteristics of the PH descriptor can be used to reduce the complexity of machine-learning models for predicting the energy of amorphous materials. Another advantage of this descriptor is its prediction interpretability. In the case of Ridge regression, we can estimate the contribution of each birth–death pair from the value of the Ridge coefficient. Figure 7(a) shows the projection of the Ridge coefficient onto the mesh grid used to generate the 2D histogram of the PD. The birth–death pairs in the dark blue region (the large-negative-coefficient region) correspond to the local structures that reduce the energy. By contrast, those in the dark red region (the large-positive-coefficient region) correspond to the local structures that increase the energy. In this study, we define the birth–death pairs in the region where the Ridge coefficient is larger (lower) than 0.003 (−0.0045) as the local structures with high (low) energy.

We then determined the local structures that correspond to the high- and low-energy regions obtained by inverse analysis based on stable volumes. Figure 7(b) shows a visualization of the high- and low-energy regions in the structure obtained from the equilibrium MD trajectory at 5000 K with a mass density of 2.4 g/cm³.

The same analysis was conducted on the remaining 24 samples obtained from the same trajectory. Figures 7(c) and 7(d) show the distributions of the birth–death times of the cycles assigned to the high- and low-energy regions. Examples of the ring structures are shown in the insets.

The distribution of the birth–death pairs for the low-energy region overlaps with the vertical line structure in Fig. 2(e), which characterizes the evolution of the MRO in the amorphous phase. By contrast, the distribution of the birth–death pairs for the high-energy region overlaps with that obtained from the liquid state, characterized by more distorted ring structures.

We also analyzed the histograms of the bond lengths and angles in the low- and high-energy regions, as shown in Figs. 7(e) and 7(f). The histograms clearly show differences between the local structures assigned to the low- and high-energy regions. In the bond length histogram, the low-energy structures exhibited a sharp peak at ~1.5 Å, whereas the peak for the high-energy structures was significantly broader. The histograms of the bond angles for the low- and high-energy structures differ in the range between 50° and 80°. These differences in the histograms indicate that high-energy structures exhibit greater randomness in terms of bonds and angles.

These analyses indicate that the regression model for energy prediction based on PDs focuses on the following two local structures as descriptors of the low- and high-energy regions: (1) large ring structures with low variation in bond length and angles, corresponding to the evolution of MRO, and (2) ring structures with greater randomness. These results verify the ability of PH to

effectively extract the correlation between geometric and topological structures and their energies.

IV. CONCLUSION

In this study, we demonstrated that the descriptors obtained from PH can predict the mean energy per atom in aC using a simple ridge regression model. The prediction accuracy was improved by utilizing a CNN model. Furthermore, we compared the results with those obtained using other methods. As examples of a conventional handcrafted representation and a GNN model, we used SOAP and SchNet, respectively. We demonstrated that the PH descriptor and latent space in the trained SchNet model exhibited similar characteristics. We visualized this point using the dimensionality reduction of the descriptor spaces obtained from PH, SOAP, and SchNet. The t-SNE 2D maps of the SOAP and SchNet descriptor spaces exhibited island-like structures. However, the distribution of each island for SchNet was significantly broader than that for SOAP, and several islands partially overlapped. The 2D visualizations of the PH descriptor space exhibited continuous distributions. A similar result was observed for the 2D maps obtained by PCA. The difference between the SOAP and PH/SchNet descriptor spaces originates from the information on the topological structure, which is intrinsically incorporated into PH and GNN.

Another advantage of the PH descriptor is the interpretability of prediction. Local structures corresponding to the high- and low-energy regions can be determined by utilizing the inverse analysis technique for PH.

In summary, the PH descriptor provides several advantages including a simple model architecture for predicting energy, the absence of hyperparameter tuning in descriptor construction, and the interpretability of prediction. However, several of these aspects require further investigation. First, a method to improve prediction accuracy is required because the accuracy of prediction by PH is not superior to that of the other methods. One possible reason for this is that PH may lack detailed geometrical information. The complementary use of PH and conventional descriptors may be a promising approach. Second, to apply this approach to large-scale molecular dynamics simulations, an extension to the prediction of the forces acting on the atoms is necessary. This would necessitate the development of PH-based techniques for extracting local topological characteristics of atom environments and the utilization of the PD derivatives with respect to atomic coordinates.

Another aspect is the construction of PH descriptors for multi-element systems. In the case of mono-element systems, such as the amorphous carbon studied here, we can obtain descriptors suitable for energy prediction by applying a filtration process in which the radii of all spheres are uniformly increased. However, when the system includes different elements, special measures are required to extract structural features that reflect the variations in the interactions between atoms of the same and different species. This problem may be solved simply by varying the initial radii of the spheres used in filtration according to the atomic species. For our proposed CNN-based model, it is also possible to combine the PD data for the partial

atomic coordinates of each element, similar to the RGB channels in the image data. The exploration of these possibilities is expected to improve machine-learning potentials based on descriptors that depict both topological and geometrical information.

SUPPLEMENTARY MATERIAL

1. Hyperparameter optimization for SOAP descriptor
2. Diversity of neighboring condition of carbon atoms in the dataset
3. Limitations originating from the use of periodic boundary conditions
4. Structures and PDs for liquid and amorphous carbon with low and high densities
5. Prediction results by PH descriptor for the dataset including crystal data
6. Prediction results by SOAP+NN model with hyperparameters different from optimal values
7. Calculation results of the energies using empirical potentials
8. Results of prediction using average values of SOAP and SchNet descriptors
9. Results of t-SNE with perplexity = 10.0
10. Results of t-SNE with perplexity = 50.0
11. Dimensional reduction analyses for SOAP descriptor space with different hyperparameters

ACKNOWLEDGMENTS

This study was supported by PRESTO Grants (Grant Nos. JPMJPR1923 and JPMJPR2198), JST, and KAKENHI Grant (Nos. 23H04470, 23H04100, 22H05106, 21H01816, 21H05552, 19H02544, 19H00834, and 20H05884), MEXT, Japan. The calculations were performed using a computer facility at the Research Center for Computational Science (Okazaki, Japan).

AUTHOR DECLARATIONS

Conflict of Interest

The authors have no conflicts to disclose.

Author Contributions

Emi Minamitani: Conceptualization (lead); Funding acquisition (equal); Investigation (lead); Methodology (lead); Software (equal); Validation (lead); Writing – original draft (lead); Writing – review & editing (equal). **Ippei Obayashi:** Conceptualization (supporting); Funding acquisition (equal); Investigation (supporting); Methodology (supporting); Software (equal); Writing – original draft (supporting); Writing – review & editing (equal). **Koji Shimizu:** Conceptualization (supporting); Investigation (supporting); Methodology (supporting); Writing – original draft (supporting); Writing – review & editing (supporting). **Satoshi Watanabe:** Conceptualization (supporting); Funding acquisition (equal); Investigation (supporting); Methodology (supporting); Writing – original draft (supporting); Writing – review & editing (supporting).

DATA AVAILABILITY

The data that support the findings of this study are openly available in Zenodo at <https://doi.org/10.5281/zenodo.7905585>. Raw data were generated at Research Center for Computational Science (Okazaki, Japan). Derived data supporting the findings of this study are available from the corresponding author upon reasonable request.

REFERENCES

- ¹W. J. Szlachta, A. P. Bartók, and G. Csányi, “Accuracy and transferability of Gaussian approximation potential models for tungsten,” *Phys. Rev. B* **90**(10), 104108 (2014).
- ²A. P. Bartók, M. C. Payne, R. Kondor, and G. Csányi, “Gaussian approximation potentials: The accuracy of quantum mechanics, without the electrons,” *Phys. Rev. Lett.* **104**(13), 136403 (2010).
- ³J. Behler and M. Parrinello, “Generalized neural-network representation of high-dimensional potential-energy surfaces,” *Phys. Rev. Lett.* **98**(14), 146401 (2007).
- ⁴J. S. Smith, O. Isayev, and A. E. Roitberg, “ANI-1: An extensible neural network potential with DFT accuracy at force field computational cost,” *Chem. Sci.* **8**(4), 3192–3203 (2017).
- ⁵K. T. Schütt, P.-J. Kindermans, H. E. Sauceda, S. Chmiela, A. Tkatchenko, and K.-R. Müller, “SchNet: A continuous-filter convolutional neural network for modeling quantum interactions,” *Adv. Neural Inf. Process. Syst.* **30**, 992–1002 (2017).
- ⁶J. Gilmer, S. S. Schoenholz, P. F. Riley, O. Vinyals, and G. E. Dahl, “Neural message passing for quantum chemistry,” [arXiv:1704.01212](https://arxiv.org/abs/1704.01212) (2017).
- ⁷A. P. Thompson, L. P. Swiler, C. R. Trott, S. M. Foiles, and G. J. Tucker, “Spectral neighbor analysis method for automated generation of quantum-accurate interatomic potentials,” *J. Comput. Phys.* **285**, 316–330 (2015).
- ⁸V. Botu, R. Batra, J. Chapman, and R. Ramprasad, “Machine learning force fields: Construction, validation, and outlook,” *J. Phys. Chem. C* **121**(1), 511–522 (2017).
- ⁹A. V. Shapeev, “Moment tensor potentials: A class of systematically improvable interatomic potentials,” *Multiscale Model. Simul.* **14**(3), 1153–1173 (2016).
- ¹⁰L. Zhang, J. Han, H. Wang, R. Car, and W. E, “Deep potential molecular dynamics: A scalable model with the accuracy of quantum mechanics,” *Phys. Rev. Lett.* **120**(14), 143001 (2018).
- ¹¹J. Gasteiger, J. Groß, and S. Günnemann, “Directional message passing for molecular graphs,” [arXiv:2003.03123](https://arxiv.org/abs/2003.03123) (2020).
- ¹²O. T. Unke and M. Meuwly, “PhysNet: A neural network for predicting energies, forces, dipole moments, and partial charges,” *J. Chem. Theory Comput.* **15**(6), 3678–3693 (2019).
- ¹³A. P. Bartók, R. Kondor, and G. Csányi, “On representing chemical environments,” *Phys. Rev. B* **87**(18), 184115 (2013).
- ¹⁴J. Behler, “Atom-centered symmetry functions for constructing high-dimensional neural network potentials,” *J. Chem. Phys.* **134**(7), 074106 (2011).
- ¹⁵A. J. Zomorodian, *Topology for Computing* (Cambridge University Press, 2005).
- ¹⁶H. Edelsbrunner and J. Harer, *Computational Topology: An Introduction* (American Mathematical Society, Providence, RI, 2010).
- ¹⁷T. Nakamura, Y. Hiraoka, A. Hirata, E. G. Escobar, and Y. Nishiura, “Persistent homology and many-body atomic structure for medium-range order in the glass,” *Nanotechnology* **26**(30), 304001 (2015).
- ¹⁸Y. Hiraoka, T. Nakamura, A. Hirata, E. G. Escobar, K. Matsue, and Y. Nishiura, “Hierarchical structures of amorphous solids characterized by persistent homology,” *Proc. Natl. Acad. Sci. U. S. A.* **113**(26), 7035–7040 (2016).
- ¹⁹S. S. Sørensen, T. Du, C. A. N. Biscio, L. Fajstrup, and M. M. Smedskjaer, “Persistent homology: A tool to understand medium-range order glass structure,” *J. Non-Cryst. Solids: X* **16**, 100123 (2022).
- ²⁰Z. Meng, D. V. Anand, Y. Lu, J. Wu, and K. Xia, “Weighted persistent homology for biomolecular data analysis,” *Sci. Rep.* **10**(1), 2079 (2020).
- ²¹S. S. Sørensen, C. A. N. Biscio, M. Bauchy, L. Fajstrup, and M. M. Smedskjaer, “Revealing hidden medium-range order in amorphous materials using topological data analysis,” *Sci. Adv.* **6**(37), eabc2320 (2020).

- ²²S. Hong and D. Kim, "Medium-range order in amorphous ices revealed by persistent homology," *J. Phys.: Condens. Matter* **31**(45), 455403 (2019).
- ²³E. Minamitani, T. Shiga, M. Kashiwagi, and I. Obayashi, "Relationship between local coordinates and thermal conductivity in amorphous carbon," *J. Vac. Sci. Technol. A* **40**(3), 033408 (2022).
- ²⁴E. Minamitani, T. Shiga, M. Kashiwagi, and I. Obayashi, "Topological descriptor of thermal conductivity in amorphous Si," *J. Chem. Phys.* **156**, 244502 (2022).
- ²⁵A. S. Krishnapriyan, J. Montoya, M. Haranczyk, J. Hummelshøj, and D. Morozov, "Machine learning with persistent homology and chemical word embeddings improves prediction accuracy and interpretability in metal-organic frameworks," *Sci. Rep.* **11**(1), 8888 (2021).
- ²⁶X. Chen, D. Chen, M. Weng, Y. Jiang, G.-W. Wei, and F. Pan, "Topology-based machine learning strategy for cluster structure prediction," *J. Phys. Chem. Lett.* **11**(11), 4392–4401 (2020).
- ²⁷S. M. Moosavi, H. Xu, L. Chen, A. I. Cooper, and B. Smit, "Geometric landscapes for material discovery within energy-structure-function maps," *Chem. Sci.* **11**(21), 5423–5433 (2020).
- ²⁸Y. Jiang, D. Chen, X. Chen, T. Li, G. W. Wei, and F. Pan, "Topological representations of crystalline compounds for the machine-learning prediction of materials properties," *npj Comput. Mater.* **7**(1), 28 (2021).
- ²⁹J. Townsend, C. P. Micucci, J. H. Hymel, V. Maroulas, and K. D. Vogiatzis, "Representation of molecular structures with persistent homology for machine learning applications in chemistry," *Nat. Commun.* **11**(1), 3230 (2020).
- ³⁰G. Kresse and J. Hafner, "Ab initio molecular dynamics for liquid metals," *Phys. Rev. B* **47**(1), 558 (1993).
- ³¹G. Kresse and J. Furthmüller, "Efficiency of ab-initio total energy calculations for metals and semiconductors using a plane-wave basis set," *Comput. Mater. Sci.* **6**(1), 15–50 (1996).
- ³²G. Kresse and J. Furthmüller, "Efficient iterative schemes for ab initio total-energy calculations using a plane-wave basis set," *Phys. Rev. B* **54**(16), 11169 (1996).
- ³³G. Kresse and D. Joubert, "From ultrasoft pseudopotentials to the projector augmented-wave method," *Phys. Rev. B* **59**(3), 1758 (1999).
- ³⁴S. Nosé, "A unified formulation of the constant temperature molecular dynamics methods," *J. Chem. Phys.* **81**(1), 511–519 (1984).
- ³⁵W. G. Hoover, "Canonical dynamics: Equilibrium phase-space distributions," *Phys. Rev. A* **31**(3), 1695–1697 (1985).
- ³⁶I. Obayashi, T. Nakamura, and Y. Hiraoka, "Persistent homology analysis for materials Research and persistent homology software: HomCloud," *J. Phys. Soc. Jpn.* **91**(9), 091013 (2022).
- ³⁷See <https://homcloud.dev/index.en.html> for HomCloud.
- ³⁸H. Adams, T. Emerson, M. Kirby, R. Neville, C. Peterson, P. Shipman, S. Chepushtanova, E. Hanson, F. Motta, and L. Ziegelmeier, "Persistence images: A stable vector representation of persistent homology," *J. Mach. Learn. Res.* **18**(8), 1–35 (2017).
- ³⁹I. Obayashi, Y. Hiraoka, and M. Kimura, "Persistence diagrams with linear machine learning models," *J. Appl. Comput. Topol.* **1**(3–4), 421–449 (2018).
- ⁴⁰I. Obayashi, "Volume-optimal cycle: Tightest representative cycle of a generator in persistent homology," *SIAM J. Appl. Algebra Geom.* **2**(4), 508–534 (2018).
- ⁴¹I. Obayashi, "Stable volumes for persistent homology," *J. Appl. Comput. Topol.* (published online 2023).
- ⁴²L. Himanen, M. O. J. Jäger, E. V. Morooka, F. Federici Canova, Y. S. Ranawat, D. Z. Gao, P. Rinke, and A. S. Foster, "DScribe: Library of descriptors for machine learning in materials science," *Comput. Phys. Commun.* **247**, 106949 (2020).
- ⁴³T. Akiba, S. Sano, T. Yanase, T. Ohta, and M. Koyama, in *Proceedings of the 25th ACM SIGKDD International Conference on Knowledge Discovery & Data Mining* (Association for Computing Machinery, New York, 2019), pp. 2623–2631.
- ⁴⁴K. T. Schütt, P. Kessel, M. Gastegger, K. A. Nicoli, A. Tkatchenko, and K.-R. Müller, "SchNetPack: A deep learning toolbox for atomistic systems," *J. Chem. Theory Comput.* **15**(1), 448–455 (2019).
- ⁴⁵F. Pedregosa, G. Varoquaux, A. Gramfort, V. Michel, B. Thirion, O. Grisel, M. Blondel, P. Prettenhofer, R. Weiss, V. Dubourg, J. Vanderplas, A. Passos, D. Cournapeau, M. Brucher, M. Perrot, and É. Duchesnay, "Scikit-learn: Machine learning in Python," *J. Mach. Learn. Res.* **12**(85), 2825–2830 (2011).
- ⁴⁶A. Paszke, S. Gross, F. Massa, A. Lerer, J. Bradbury, G. Chanan, T. Killeen, Z. Lin, N. Gimelshein, L. Antiga, A. Desmaison, A. Kopf, E. Yang, Z. DeVito, M. Raison, A. Tejani, S. Chilamkurthy, B. Steiner, L. Fang, J. Bai, and S. Chintala, "PyTorch: An imperative style, high-performance deep learning library," *Adv. Neural Inf. Process. Syst.* **32**, 8024–8035 (2019).